

International Conference on Space Optics—ICSO 2022

Dubrovnik, Croatia

3–7 October 2022

Edited by Kyriaki Minoglou, Nikos Karafolas, and Bruno Cugny,



Ka- and lower Q-band, high responsivity, packaged RF photodiode



Ka- and lower Q-band, high responsivity, packaged RF photodiode

S. Watanabe, W. Quan, C. Petit, H. Meier*^a

^aAlbis Optoelectronics AG, Moosstrasse 2a, 8803 Rueschlikon, Switzerland

ABSTRACT

We demonstrate a small size and low weight packaged photodiode for space-based photonic RF applications. The photodiode offers a broadband 50Ω matching, a 3 dB-bandwidth above 40 GHz and a linear response up to +10 dBm optical input power with a responsivity of 0.75 A/W.

Keywords: photodiode, photonics payload, microwave, RoF, APL, linearity, Ka-band, Q-band

1. INTRODUCTION

Photonic enabled satellite payloads¹ demonstrate potentially superior performance and improved size, weight and power (SWaP) consumption. In comparison with regular electrical RF cables, the use of fiber optics in satellites increases flexibility, simplifies harness routing, decreases the susceptibility to electro-magnetic interference (EMI) and allows low loss transparent transmission at high frequencies over large distances. In the last decades, photonic technologies have been widely used in various radio over fiber (RoF) or analogue photonic link (APL) systems. More recent applications include the distribution of RF signals to remote radio heads (RRH) for 5G mobile fronthaul and beyond², indoor distributed antenna systems (DAS)³, radar⁴, phased array antennas for optical beam forming⁵ and radio astronomy⁶. Microwave photonics is used in synthesis of RF signals⁷ which can be used as low noise local oscillators⁸.

A core component in any microwave photonic application is a photodiode converting an optical into an electrical RF signal. As the noise figure of an intensity modulated direct-detection (IMDD) APL tends to improve inversely proportional to average photocurrent in the detector^{9,10}, high optical power handling photodiodes are desired¹¹. Advanced uni-traveling-carrier (UTC) type photodiodes^{12,13,14} offer high potential RF output power and can be optimized to generate signals with extremely high linearity¹⁵.

For many applications in Ka- and Q-band a linear response of the detector up to an optical input power of +10 dBm is required. In such operation regime, detectors based on PIN photodiodes offer better responsivity compared to UTC photodiodes. In this work, we demonstrate the performance of a packaged, high speed InGaAs/InP, 40 GHz PIN photodiode for applications in Ka- and lower Q-band. The package is optimized for small size and low weight, making it attractive for spaceborne application. A main challenge in packaging high speed photodetectors is to minimize the optical coupling losses between the optical fiber input and the photodetector. In this work, we use a backside illuminated high speed photodiode featuring a backside, monolithically integrated lens. This backside lens enables an optimized optical system with high optical coupling efficiency and large alignment tolerances, making it possible to fabricate packaged photodiodes with low coupling losses in a cost efficient manner. As a result, very high speed photodiodes with small active diameter and capacitance can be used, enabling high frequency operation.

*hektor.meier@albisopto.com, www.albisopto.com

2. PACKAGED RF PHOTODIODE

2.1 Photodiode

The detector used in this work is an InGaAs/InP high speed PIN photodiode chip (PD40X1, see Figure 1). The detection area as well as the GSG connection pads are located on the front side of the chip. On the backside of the InP substrate, the light entry area features a monolithically integrated spherical lens with anti-reflective coating reducing reflection of the optical interface below 1% at the specified wavelength. The position of the lens with respect to the top side detection area is aligned with photolithographic precision, better than $\pm 2 \mu\text{m}$. The lens enables high optical coupling efficiency, increased alignment tolerances and can be optimized for specific optical illumination system requirements. The photodiode offers a responsivity of $R_{\text{PD}} = 0.82 \text{ A/W}$ at wavelength $\lambda = 1550 \text{ nm}$ and $T = 25 \text{ }^\circ\text{C}$ without polarization dependent losses while the small front side active area provides a low capacitance of $C_{\text{PD}} = 40 \text{ fF}$ and high 3 dB-bandwidth of $f_{3\text{dB,PD}} = 38 \text{ GHz}$ measured on 50Ω load on a probe station¹.

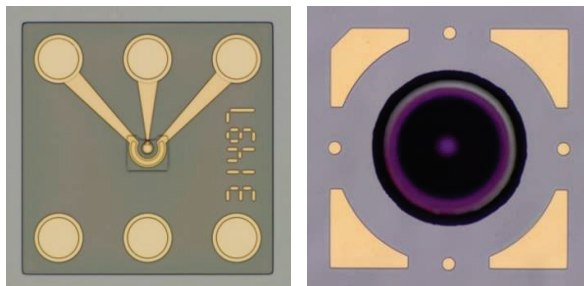


Figure 1. 56 Gbd InGaAs/InP photodiode chip PD40X1, Left: front side with GSG pad layout. The vertical illuminated active element is in the centre of the chip, Right: backside with monolithically integrated, spherical lens with anti-reflective coating.

2.2 Fabrication

The fully tested photodiode chip PD40X1 is flip-chip soldered on an Al_2O_3 ceramic carrier using an eutectic solder process. The ceramic includes a resistive broadband 50Ω matching circuit as well as a bias-T circuitry. This sub-assembly is soldered into the package body. Then, the optical fiber is actively aligned to the photodiode to optimize responsivity and linearity. The optical feedthrough is hermetically sealed. After functional testing, the lid of the package is hermetically sealed, and its hermeticity is tested in a gross and fine leak test. The resulting packaged photodiode PQS40A-L is shown in Figure 2.



Figure 2. Packaged RF photodiode PQS40A-L.

2.3 Packaged Photodiode Description

PQS40A-L features an optical single mode fiber pigtail with an FC/APC connector. The DC coupled RF output is provided through a K-connector. The photodiode reverse bias voltage is applied through the internal bias-T (see Figure 3 for the schematic pin configuration). The package is specifically optimized for small size and low weight ($< 8 \text{ g}$ without fiber pigtail). The dimensions are shown in Figure 3.

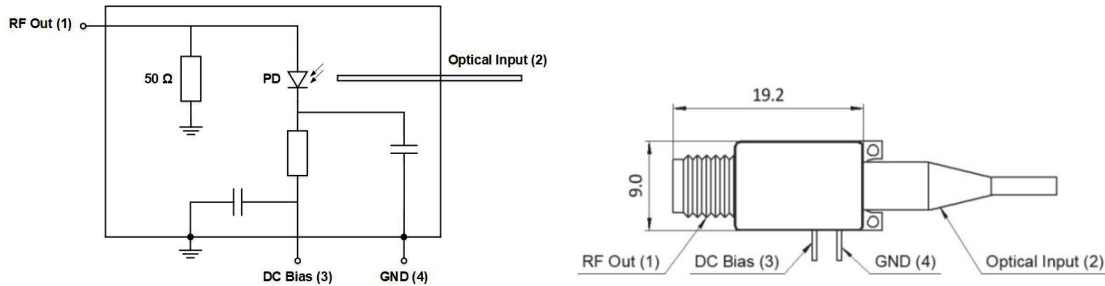


Figure 3. Left: Schematic pin configuration of PQS40A-L. Right: Mechanical dimensions (in μm) of PQS40A-L. The package height is 9.1 μm .

3. MEASUREMENT RESULTS

3.1 Responsivity

Responsivity of the packaged photodiode is measured using a continuous wave (CW) laser with wavelength of $\lambda = 1550 \text{ nm}$. The optical power is controlled and calibrated in front of the optical connector of PQS40A-L using an Agilent N7752A optical attenuator. In order to measure the temperature dependence, the device under test (DUT) is placed in a Vötsch VT4002 climate chamber. We obtain a responsivity of $R = 0.75 \text{ A/W}$ at wavelength $\lambda = 1550 \text{ nm}$, $T = 25 \text{ }^\circ\text{C}$ and reverse bias voltage $V_B = 5 \text{ V}$. Compared to the responsivity of PD40X1, we estimate the coupling efficiency between the FC/APC connector and photodiode chip to be around 91%. The responsivity decreases at lower temperature. The optical return loss (ORL) is better than 40 dB over the entire temperature range, indicating stable optical coupling.

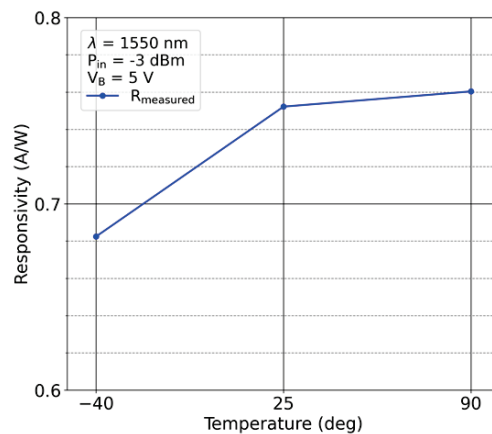


Figure 4 Responsivity measurement result of PQS40A-L as a function of temperature.

3.2 S-Parameter

The S-parameters of PQS40A-L are measured by the setup shown in Figure 5. The electrical RF signal from the vector network analyser (VNA) is used to generate an optically modulated signal using a LiNbO_3 modulator. The modulated optical signal at wavelength $\lambda = 1550 \text{ nm}$ has an extinction ratio (ER) around 14 dB. The optical signal is transmitted through an optical attenuator to the optical input of PQS40A-L (port #2). The average optical input power is approximately $P_{in} \sim -3 \text{ dBm}$. The electrical RF output signal (port #1) is directly connected to the VNA, while the bias voltage is applied through an external power supply to the DC bias pin (port #3). In order to measure the temperature dependence, the DUT is placed in a climate chamber, which allows to control the temperature between $-40 \text{ }^\circ\text{C}$ and $90 \text{ }^\circ\text{C}$ in ambient atmosphere.

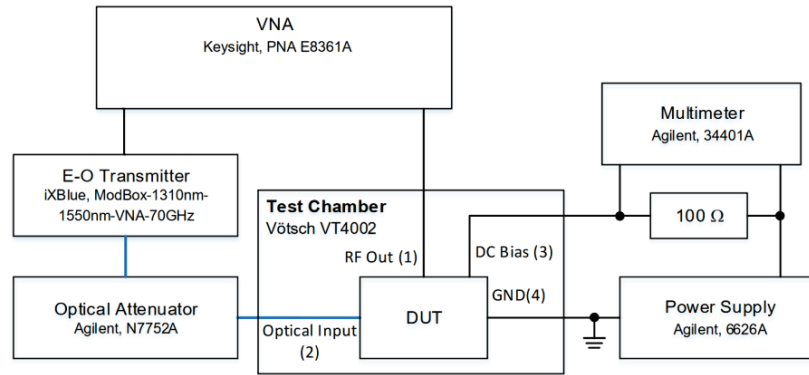


Figure 5. O/E S-parameter measurement setup.

The frequency response (S_{12}) at wavelength $\lambda = 1550$ nm and electrical return loss (S_{11}) are shown in Figure 6. The response is flat over the entire frequency up to 38 GHz with a 3 dB-bandwidth above 40 GHz. The broadband response of this component in combination with its high responsivity enables operation in C-, X-, Ku- and the entire Ka-band (26.5 GHz to 40 GHz) as well as in the lower portion of the Q-band (37.5 GHz to 42.5 GHz). The electrical return loss $\text{Mag}(S_{11})$ remains below -5 dB up to 34 GHz.

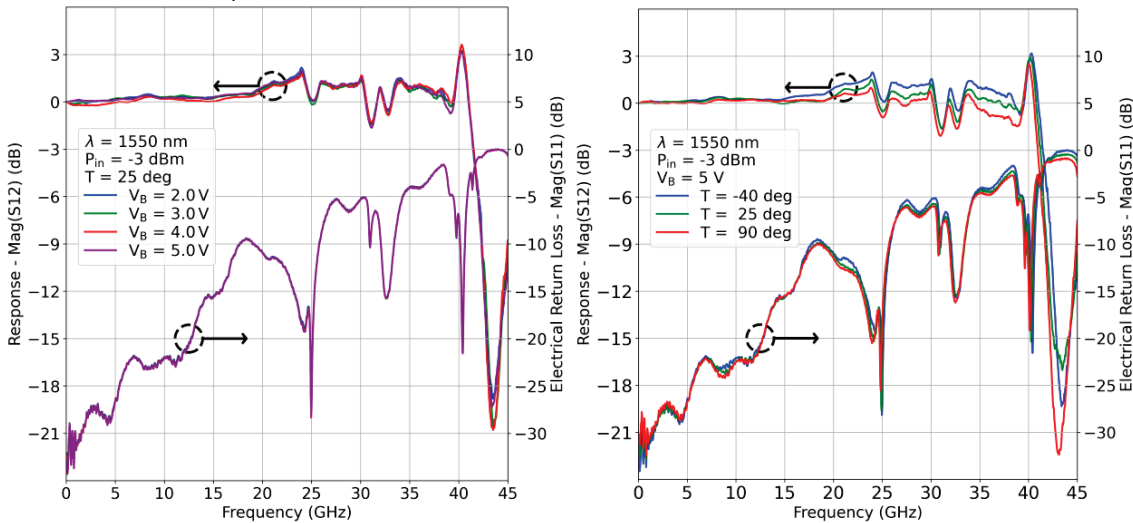


Figure 6. Frequency response (S_{12}) and electrical return loss (S_{11}) measurement of PQS40A-L. Left: As a function of applied DC bias voltage V_B . Right: As function of temperature.

The frequency response of PQS40A-L shows only a small bias voltage dependence since the photodiode chip is fully depleted above $V_B = 1.0$ V, meaning the device capacitance and transit time does not change significantly under higher reverse bias voltage. The temperature dependence of the frequency response is small.

3.3 Linearity

We define the linear regime of the photodiode by measuring the 1 dB compression point at a fixed RF frequency. The linear region is determined as a function of the RF output vs. the RF input power where the RF output power at the fundamental frequency decreases by 1 dB or 10 % from its linear relationship with respect to the RF input power. Above this point the photodiode goes into optical saturation and generates higher order harmonics and non-linearities. The optical RF input power is a function of its ER and is proportional to the average optical input power which is itself proportional to the average photocurrent generated by the photodiode. Therefore, for a fixed ER, it is common to describe the linearity

of the photodiode by the average photocurrent at the 1 dB compression point. We call this photocurrent the optical saturation current I_s ¹⁶.

The linearity of PQS40A-L is measured using the setup shown in Figure 7. The VNA generates an electrical RF signal at a fixed frequency which drives a LiNbO₃ modulator to generate an optical signal at the wavelength $\lambda = 1550$ nm. In order to obtain the necessary optical RF power, the signal is first amplified using an erbium doped fiber amplifier (EDFA) and then the average optical power is controlled using an optical attenuator. The electrical RF output of the DUT (port #1) is measured using the VNA at the operating frequency. The bias voltage is applied using a power supply while the photocurrent is measured by the bias voltage drop across a 100 Ω resistor in the biasing circuit. In order to guarantee a fixed, nominal bias voltage at the DUT (port #3), the voltage drop across the 100 Ω resistor is compensated by increasing the voltage of the power supply as a function of the average photocurrent at every optical input power.

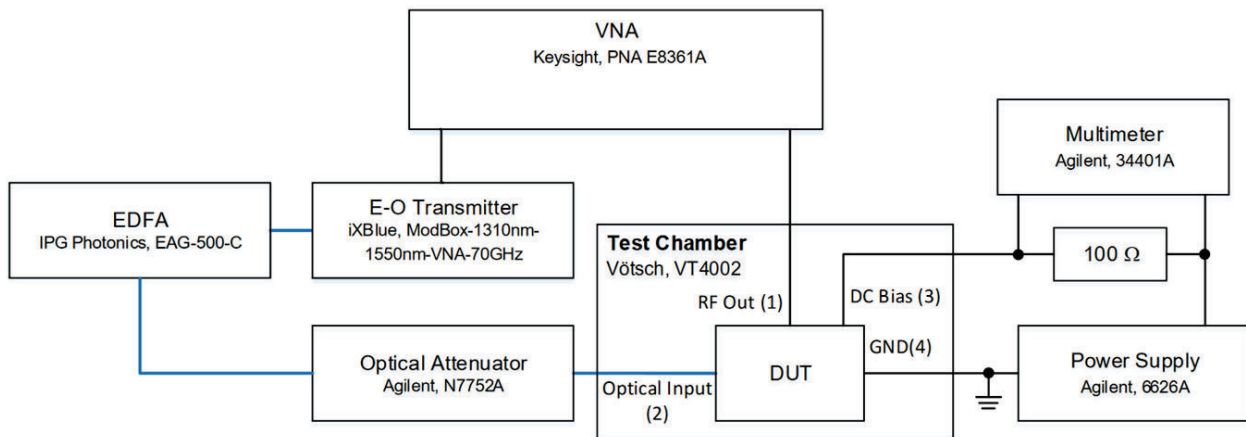


Figure 7. 1 dB compression point measurement setup.

The linearity measurement at a fixed frequency of $f = 40$ GHz is shown in Figure 8. Increasing the average optical input power results in a linear increase of the average photocurrent flowing through the photodiode. Above the optical saturation current I_s , the optical power density on the photodiode active diameter is high enough to create very high density of electron-hole pairs which screen the applied electric field, known as space-charge effect¹⁷. As a result, carrier transport is slowed down, the photodiode bandwidth decreases, and non-linearities in the response of the detector are introduced. This detrimental effect depends first and foremost on the optical power density on the detector¹⁸. In order to increase the linear range, the optical power density should be as uniform as possible over the detecting area. Considering that the main design target of this photodiode is to optimize optical coupling and responsivity, overfilling of the active element with the optical spot size to create a more uniform optical power density profile is not an option¹⁹ and optical beam shaping²⁰ is difficult to implement for small area detectors in such small package. Therefore, we have focussed our effort on increasing the spot size by tightly controlling the fiber position and the lens shape of the monolithically integrated backside lens, reducing the non-spherical aberrations. This avoids distortion to the Gaussian optical power density profile created by the single mode fiber illumination and hence makes the optical power distribution reproducible.

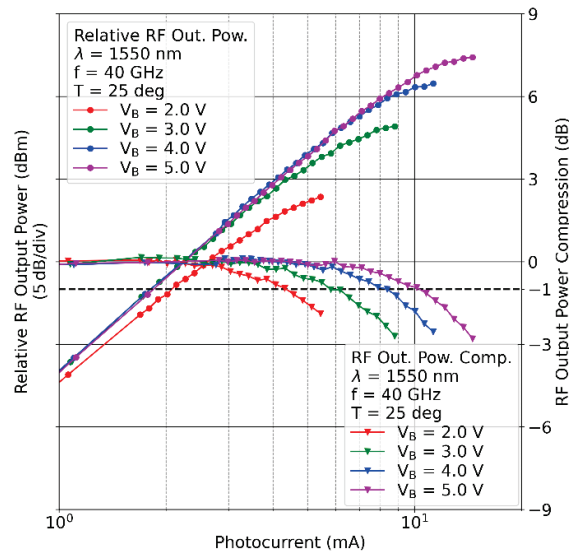


Figure 8. Left axis Change of the RF output power of PQS40A-L at $f = 40$ GHz as a function of measured average photocurrent and applied DC bias voltage V_B . Right axis shows the compression of the relative RF output power with respect to a linear relationship.

A further effect which reduces the optical saturation current is a photocurrent dependent voltage drop caused by the 80Ω resistor as part of the bias-T (see Figure 3) and the 50Ω load resistance in parallel with the 50Ω matching termination. The series resistance of the photodiode itself also causes an electric field drop in the junction²¹. However, this effect is minor considering the photocurrents are in orders of tens of mA and the series resistance of the photodiode is only around 7Ω , extracted from S_{11} measurement of the photodiode chip. The bias voltage drop lowers the available bias across the photodiode and hence the field inside the junction²². Therefore, less charge or optical input power is required to create the space-charge effect. Furthermore, the on-set of optical saturation effect is temperature dependent. At higher temperature, the mobility of the charge carriers, in particular for holes, decreases. It inhibits transport of the carrier from the junction which feeds back to enhanced charge accumulation which typically starts on the n-side of the depletion region¹⁷. These dependencies can be observed in the measured temperature and bias voltage dependence of the optical saturation current shown in Figure 9. At $V_B = 5$ V and $T = 90^\circ\text{C}$, linear operation at $f = 40$ GHz is maintained up to $I_s = 8$ mA corresponding to an average optical input power of approximately $P_{in} \sim +10.2$ dBm considering the measured responsivity shown in Figure 4. The linear operation regime increases for decreasing temperature to $I_s = 10$ mA ($P_{in} \sim +11.2$ dBm) and $I_s = 12$ mA ($P_{in} \sim +12.5$ dBm), at $T = 25^\circ\text{C}$ and $T = -40^\circ\text{C}$, respectively. These photocurrents result only in moderate dissipated power $P = I_s V_B \sim 50$ mW in the junction of the photodiode, and therefore thermal runaway¹⁸ and catastrophic failure are not a concern. The optical saturation current is only slightly frequency-dependent as seen in Figure 9, which indicates that the optical saturation mechanism mostly depends on the average photocurrent.

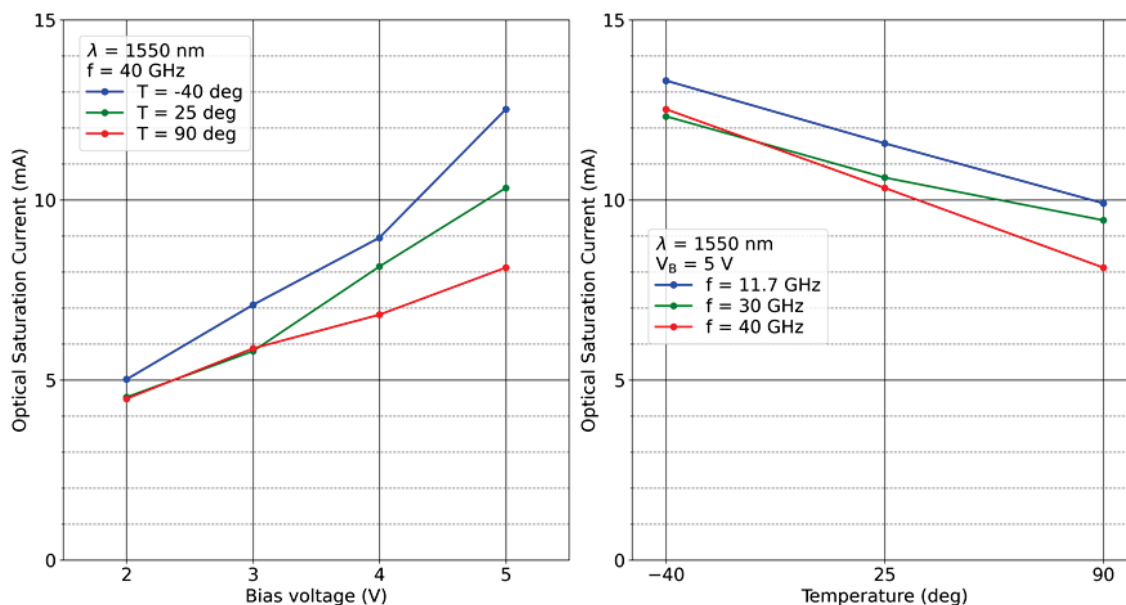


Figure 9. Left: Bias voltage and temperature dependence of optical saturation current at $f = 40 \text{ GHz}$. Right: Temperature dependence of optical saturation current at three different frequencies.

4. CONCLUSION

We demonstrated a packaged, high speed photodiode PQS40A-L with a 3 dB-bandwidth above 40 GHz and responsivity of 0.75 A/W. To the best of our knowledge, the combination of such high bandwidth and responsivity exceeds any broadband, hermetically packaged PIN photodiodes that are currently commercially available. This performance is enabled through the backside, monolithically integrated lens of the high speed, high responsivity photodiode chip which allows for active optical alignment with minimal coupling losses. Furthermore, PQS40A-L exhibits high linearity at 40 GHz with optical saturation currents between 12 mA to 8 mA in the temperature range from $-40 \text{ }^\circ\text{C}$ to $90 \text{ }^\circ\text{C}$. The small form factor and low weight make this device ideally suited for spaceborne photonic RF applications in the C-, X-, Ku-, Ka- and lower parts of the Q-band. Preliminary qualification tests are on-going. A technology readiness level (TRL) 7 is aimed to be achieved by the end of 2023.

Acknowledgment: We thank Fabienne Schaub, Valeria Liverini and Sandro Rusterholz for their contributions in this project.

Research funding: This work was conducted within the framework of the H2020-SPACE-SIPHODIAS project, and funding was received from the Horizon 2020 Research and Innovation Programme of the European Union under Grant Agreement No. 870522.

Conflict of interest: The authors declare no conflicts of interest regarding this contribution.

REFERENCES

- ¹ Sourikopoulos, I., Stampoulidis, L., Giannakopoulos, S., Zirath, H., Ostrovskyy, P., Fischer, G., Faugeron, M., Maho, A., Cyrille, L., Bouisset, G., Venet, N., Sotom, M., Irion, M., Schaub, F., Barbero, J., Lopez, D., Walker, R. G., Zhou, Y., Oxtoby, I., Duffy, S., "The H2020-SPACE-SIPHODIAS project: space-grade opto-electronic interfaces for photonic digital and analogue very-high-throughput satellite payloads," Proc. SPIE 11852, International Conference on Space Optics — ICSO 2020, 1185254 (2021); <https://doi.org/10.1117/12.2599927>
- ² Lim, C., Nirmalathas, A., "Radio-Over-Fiber Technology: Present and Future," J. Lightwave Technol. 39, 881-888 (2021)
- ³ Moon, S. R., Sung, M., Kim, E. S., Lee, J. K., Cho, S. H., and Kim, J., "RoF-based indoor distributed antenna system that can simultaneously support 5G mmWave and 6G terahertz services," Opt. Express 30, 1521-1533 (2022)
- ⁴ Ghelfi, P. et al., "Photonics in Radar Systems: RF Integration for State-of-the-Art Functionality," IEEE Microwave Magazine, vol. 16, no. 8, pp. 74-83, (2015), doi: 10.1109/MMM.2015.2441591.
- ⁵ Duarte, V.C., Prata, J.G., Ribeiro, C.F. et al. "Modular coherent photonic-aided payload receiver for communications satellites," Nat Commun 10, 1984, (2019). <https://doi.org/10.1038/s41467-019-10077-4>
- ⁶ Perini, F., Rusticelli, S., Schiaffino, M., Mattana, A., Monari, J., Tartarini, G., Nanni, J., Juswardy, B., Wayth, R., Waterson, M., "Radio frequency over fiber technology for SKA-low receiver," J. Astron. Telesc. Instrum. Syst., 8(1), 011016, (2022), <https://doi.org/10.1117/1.JATIS.8.1.011016>
- ⁷ Xie, X., Bouchand, R., Nicolodi, D. et al. "Photonic microwave signals with zeptosecond-level absolute timing noise," Nature Photon 11, 44–47, (2017). <https://doi.org/10.1038/nphoton.2016.215>
- ⁸ Karlen, L., Torcheboeuf, N., Kundermann, S., Herr, T., Obrzud, E., Brasch, V., Schaub, F., Meier, H., Stroganov, A., Geiselmann, M., Lecomte, S., "Photonics-based ultra-low phase noise X-band microwave generation," Proc. SPIE 11852, International Conference on Space Optics — ICSO 2020, 1185246 (2021)
- ⁹ McKinney, J., Williams, K., & Sunderman, C., "Analog Photonic Links for Built-in-Testing of Electronic Support Measures", (ESM) Systems. 26, (2009)
- ¹⁰ Urick, V.J., McKinney, J.D., Williams, K.J., "Fundamentals of Microwave Photonics", John Wiley & Sons Inc., (2015).
- ¹¹ Meier, H., Schaub, F., Liverini, V., Portuondo-Campa, E., Lecomte, S., "High-power photoreceivers for large dynamic range:, high frequency photonic RF links", Proc. SPIE 11852, International Conference on Space Optics – ICSO 2020, 1185245, (2021)
- ¹² Nagatsuma, T., Ito, H., Ishibashi, T., "High-power RF photodiodes and their applications", Laser & Photonics Reviews. 3. 123 – 137, (2009).
- ¹³ Runge P. et al., "Linearity of Waveguide Integrated Modified Uni-Travelling Carrier Photodiode Arrays," in IEEE Photonics Technology Letters, vol. 31, no. 3, pp. 246-249, 1, (2019)
- ¹⁴ E. Rouvalis et al., "High-Power and High-Linearity Photodetector Modules for Microwave Photonic Applications," in Journal of Lightwave Technology, vol. 32, no. 20, pp. 3810-3816, Oct.15, (2014), doi: 10.1109/JLT.2014.2310252.
- ¹⁵ Davila-Rodriguez, J., Xie, X., Zang, J., Long, C. J., Fortier, T. M., Leopardi, H., Nakamura, T., Campbell, J.C., Diddams, S.A., and Quinlan, F., "Optimizing the linearity in high-speed photodiodes," Opt. Express 26, 30532-30545 (2018)
- ¹⁶ Beling, A., Xie, X., Campbell, J. C., "High-power, high-linearity photodiodes," Optica 3, 328-338 (2016)
- ¹⁷ Williams, K.J., Esman, R.D., Dagenais, M., "Effects of High Space-Charge Fields on the Response of Microwave Photodetectors", IEEE Photonics Technology Letters, Vol. 6, No5, (1994)
- ¹⁸ Williams, K.J., Esman, R.D., "Design Considerations for High-Current Photodetectors", Journal of Lightwave Technology, Vol. 17, No. 8, (1999)
- ¹⁹ Davis, G. A., Weiss, R. E., LaRue, R. A., Williams, K. J. and Esman, R. D., "A 920-1650-nm high-current photodetector," in IEEE Photonics Technology Letters, vol. 8, no. 10, pp. 1373-1375, (1996).
- ²⁰ Joshi, A. and Becker, D., "GRIN Lens-Coupled Top-Illuminated Photodetectors for High-Power Applications," Microwave Photonics, 2007 International Topical Meeting on, (2007)
- ²¹ Li, N., et al., "High-saturation-current charge-compensated InGaAs-InP uni-traveling-carrier photodiode," in IEEE Photonics Technology Letters, vol. 16, no. 3, pp. 864-866, (2004)
- ²² Chtioui, M., Enard, A., Carpentier, D., Lelarge, F., Rousseau, B., Achouche, M., Marceaux, A., Renoult, A., Feuillet, C., Queguiner, M., Merlet, T., "High Power UTC Photodiodes Design and Applications for Analog Fiber Optic Links", 2009 International Topical Meeting on Microwave Photonics, (2009)